Facile Synthesis of Zr-Based Functional Materials with Highly Ordered Mesoporous Structures

Quan Yuan,[†] Le-Le Li,[†] Shu-Liang Lu,[‡] Hao-Hong Duan,[†] Zhen-Xing Li,[†] Yue-Xiang Zhu,[‡] and Chun-Hua Yan*,[†]

Beijing National Laboratory for Molecular Sciences, State Key Laboratory of Rare Earth Materials Chemistry and Applications & PKU-HKU Joint Laboratory in Rare Earth Materials and Bioinorganic Chemistry and State Key Laboratory for Structural Chemistry of Unstable and Stable Species, College of Chemistry and Molecular Engineering, Peking University, Beijing 100871, China

Received: July 22, 2008; Revised Manuscript Received: October 17, 2008

A simple general method has been developed for the synthesis of Zr-based multicomponent functional materials with highly ordered mesoporous structure, including pure zirconia, ceria−zirconia solid solutions, yttria-stabilized zirconia, and scandia-stabilized zirconia. Amphiphilic poly(alkylene oxide) block copolymers serve as structure-directing agents (SDAs). More importantly, the whole process is self-adjusting to organize the network-forming metal oxide species without any additional acid or base. Small-angle X-ray diffraction (XRD) and transmission electron microscopy (TEM) measurements show that these mesoporous Zr-based materials possess 2D hexagonal mesostructure (*p*6*mm*) with large-domain order and crystalline walls. Nitrogen sorption isotherms reveal that these materials have large surface areas, pore volumes, and narrow pore size distributions. The introduction of the second metal species to the Zr-based system enhances the thermal stability of the mesostructures, and in certain cases, they are resistant to high temperature up to 700 °C. All features above of these Zr-based mesoporous materials promise the various potentials in heterogeneous catalysis, solid oxide fuel cells (SOFCs), oxygen sensors, and so forth. With the selection of the hydrogenation of benzene as a test reaction, the representative mesoporous ZrO_2 and $Ce_{0.5}Zr_{0.5}O_2$ loaded with ruthenium demonstrate their potentials in catalysis.

Introduction

Zirconia-based materials have attracted considerable interest in the fields of catalysis, fuel cell electrolytes, high-performance transformation-toughened structural engineering ceramic, electro-optical materials, gas sensors, damage-resistant optical coatings, and gate dielectrics.[1−7] Zirconia is potentially applicable in catalysis because of its redox properties as well as acidic and basic characteristics.[8,9] Ceria−zirconia is well known for distinctly improving the thermal stability, surface area, and reducibility of three-way catalysts (TWCs).[10] Therefore, CeO_2−ZrO_2 mixed oxides have gradually replaced with pure CeO_2 as oxygen storage capacity materials in TWCs since 1995.[11] Considering their good oxygen ionic conductivity, yttria-stabilized zirconia (YSZ) and scandia-stabilized zirconia (SSZ) are the materials of choice as electrolytes in the solid oxide fuel cell (SOFC).[12] Since the discovery of mesoporous silicas MCM-41,[13] great effort has been expended in the synthesis of different types of mesoporous materials (siliceous and nonsiliceous) with high surface areas and robust pore structures, which are of great importance in catalysis, gas sensors, optics, and biotechniques.[14] It is expected that mesoporous zirconia materials with large surface areas and tunable pore structures possess more attractive catalytic properties.[15]

The compositional and structural diversity of metal oxides leads to an array of unique chemical and physical properties. With advanced properties such as selective oxidation, electron or ion percolation, and energy transfer, many metal oxides are multicomponent systems containing two or more types of metal cations,[16] which have attracted attention for their potentials in electronic, (photo)catalytic, photovoltaic, and energy storage applications. To put these potentials into practice, it is necessary to control simultaneously both structure and composition on the nanoscale for these materials in a simple, inexpensive way. Furthermore, the fabrication of porous mesostructured films, powders, and monoliths from these materials is extremely important for applications in which a high interfacial surface area is required, for example, heterogeneous catalysts, photocatalysis, environmental cleaning, and solar energy conversion.[17,18] Additionally, the strategy to obtain meso-organized multimetal-oxide nanocrystals bridges the gap between conventional mesoporous materials and the remarkable properties of crystalline binary, ternary, and quaternary metallic oxides.[19] Although crystalline meso-ordered multimetallic materials have been obtained by an impregnation and inverse replica nanocasting technique with a silica or carbon host,[20,21] the direct preparation of mesoporous multimetallic oxides is complicated and difficult because of the requirement of accurate stoichiometry, highly mixable precursors, specific chemistry for each phase, and a high temperature of crystallization. Many recent efforts have been devoted to the direct synthesis of multimetallic oxides with mesostructures; however, only a few groups succeed in obtaining the well-ordered structure on the mesoscopic level.[19,22]

Over the past two decades, a variety of approaches have been developed for the preparation of mesoporous Zr-based materials. The synthesis of mesoporous zirconia with hexagonal and cubic structures was first realized by Stucky's group with triblock

* Corresponding author. Fax: +86-10-6275-4179. E-mail: yan@pku.edu.cn.
[†] State Key Laboratory of Rare Earth Materials Chemistry and Applications & PKU-HKU Joint Laboratory in Rare Earth Materials and Bioinorganic Chemistry.
[‡] State Key Laboratory for Structural Chemistry of Unstable and Stable Species.

10.1021/jp806467c CCC: $40.75
Published on Web 02/18/2009

copolymers as structure-directing agents (SDAs).[23] Schüth et al. obtained highly ordered zirconium oxide sulfate and zirconium oxophosphate with a mesostructure like that of MCM-41 and thermal stability up to 500 °C.[24] Ozin and co-workers used cetyltrimethylammonium bromide as a template to synthesize mesoporous yttria−zirconia with a high surface area (116 m^2/g) and high thermal stability.[25] However, the zirconia precursor has to be modified with ethylene glycol for the synthesis, and the process required an extended period of time (as long as 5 days).[25] Layered yttria−zirconia was fabricated by Gedanken et al. with an ultrasound irradiation method.[26] Sanchez et al. did pioneering work on ordered mesostructured $ZrO_2-Y_2O_3$ and ZrO_2-CeO_2 thin films using Pluronics polymers as a template[27] and predicted these new materials' opportunities for applications. Recently, we developed a simple method for the synthesis of highly ordered mesoporous $Ce_{1-x}Zr_xO_2$ solid solutions over a wide range of Ce/Zr ratios.[28] In particularly, the Pt-nanoparticle-loaded meso-$Ce_{0.5}Zr_{0.5}O_2$ showed interesting catalytic properties related to the mesostructure.[28]

To the best of our knowledge, no systematic, high-throughput synthesis of Zr-containing functional materials with wide M/Zr (M = Ce, Y, Sc) ratios, ordered mesostructures, and high thermal stability based on a general method has been reported. In this article, we report a direct and facile strategy for the systematic synthesis of Zr-based functional materials with a highly ordered mesoporous structure. The general synthesis strategy is based on a sol−gel process combined with evaporation-induced self-assembly (EISA) in ethanol using amphiphilic triblock copolymers as the SDAs without additional acid or base. Zirconium oxide chloride and metal nitrate were chosen as cheap precursors. Pure zirconia, ceria−zirconia, yttria-stabilized zirconia, and scandia-stabilized zirconia with ordered mesoporous stuctures and crystalline walls are systematically fabricated by finely tuning the ratio of precursors and SDAs. The M/Zr (M = Ce, Y, Sc) ratios vary in a wide range. During the synthesis procedure, we focus on the fine control of evaporation-induced self-assembly (EISA) with the temperature and the relative humidity settled, which endow all the materials a highly ordered 2D hexagonal mesostructure, large surface area, and narrow pore size distribution. The thermal stability of the mesostructures, in certain cases up to 700 °C, is enhanced with the introduction of the second metal species to the Zr-based system. These Zr-based mesoporous materials have potential applications in heterogeneous catalysts, SOFC, oxygen sensors, and so forth. Moreover, we also make some effort to explore the application of these novel materials. Loaded with ruthenium, the representative mesoporous ZrO_2 and $Ce_{0.5}Zr_{0.5}O_2$ exhibit satisfactory catalytic activity in the hydrogenation of benzene.

Experimental Section

Materials. Pluronic P123 (M_{av} = 5800, $EO_{20}PO_{70}EO_{20}$) and Pluronic F127 (M_{av} = 12 600, $EO_{106}PO_{70}EO_{106}$) were purchased from Aldrich and Sigma-Aldrich. Zirconium oxide chloride ($ZrOCl_2 \cdot 8H_2O$), cerium nitrate ($Ce(NO_3)_3 \cdot 6H_2O$), and yttrium nitrate ($Y(NO_3)_3 \cdot 6H_2O$) were purchased from Beijing Chemical Reagent Company. Scandia (Sc_2O_3) was purchased from Beijing Institute of Founder Rare Earth Sci. & Tech. Co., Ltd. All other chemicals were used as received.

Synthesis of Mesoporous ZrO_2. Pluronic F127 (0.8−1.1 g) was dissolved in 10 mL of ethanol at room temperature (RT). Then, 1.61 g (5 mmol) of $ZrOCl_2 \cdot 8H_2O$ was added to the above solution with vigorous stirring. The mixture was covered with a PE film. After being stirred for at least 2 h at room temperature, the homogeneous sol was transferred to an oven and underwent solvent evaporation. After 2 days of aging under the desired temperature and humidity (temperature 40 °C, relative humidity 50%), the gel product was dried in the other oven at 100 °C for 1 day. Calcination was carried out by slowly increasing the temperature from room temperature to 400 °C (1 °C/min ramping rate) and holding at 400 °C for 4 h in air. High-temperature treatment was carried out in air for 1 h with a temperature ramp of 10 °C/min.

Synthesis of Mesoporous $Ce_xZr_{1-x}O_2$. Generally, this is started by dissolving 0.5 g of Pluronic P123 or 0.9 g of Pluronic F127 in 10 mL of ethanol. Then quantitative amounts of $Ce(NO_3)_3 \cdot 6H_2O$ and $ZrOCl_2 \cdot 8H_2O$ are added (total amount of Ce plus Zr is 5 mmol). The following procedure is the same as that for mesoporous ZrO_2.

Syntheses of Mesoporous $Y_2O_3-ZrO_2$ and $Sc_2O_3-ZrO_2$. Mesoporous $Y_2O_3-ZrO_2$ and $Sc_2O_3-ZrO_2$ were synthesized by a procedure similar to that described above, using triblock copolymer F127 (0.5−1.0 g), $Y(NO_3)_3 \cdot 6H_2O$ ($Sc(NO_3)_3 \cdot 6H_2O$), $ZrOCl_2 \cdot 8H_2O$, and ethanol (10 mL). F127/$Y(NO_3)_3 \cdot 6H_2O$ or $Sc(NO_3)_3 \cdot 6H_2O$/$ZrOCl_2 \cdot 8H_2O$/ethanol in a molar ratio of (0.040−0.079)/(0.20−1.7)/(3.3−4.8)/2.5 was used. $Sc(NO_3)_3 \cdot 6H_2O$ was synthesized from the reaction of Sc_2O_3 and nitric acid. Sc_2O_3 (5 g) was refluxed in a mixture of 10 mL of nitric acid and 20 mL of deionized water for 12 h, and then redundant water was vaporized. The product was dried at 60 °C for 1 day.

Catalyst Preparation. All of the catalysts were prepared by the impregnation method. The $RuCl_3 \cdot 3H_2O$ (Shenyang Research Institute of Nonferrous Metals) precursor was dissolved in deionized water and impregnated into the support to produce a catalyst of 4.5 wt % Ru over supports. After the impregnation, the catalysts were dried at 110 °C for 12 h and then calcined in air at 500 °C for 4 h.

Characterization. Powder X-ray diffraction (PXRD) patterns were recorded on a Rigaku D/MAX-2000 diffractometer using Cu Kα radiation (λ = 1.5406 Å). Transmission electronic microscopy (TEM) and energy-dispersive X-ray analysis (EDAX) were carried out on a Hitachi H-9000 NAR transmission electron microscope under a working voltage of 300 kV. The nitrogen adsorption and desorption isotherms at 78.3 K were measured using an ASAP 2010 analyzer. The surface areas were calculated by Brunauer−Emmett−Teller (BET) equation. Using the Barrett−Joyner−Halenda (BJH) model, the pore volumes and pore size distributions were derived from the desorption branches of the isotherms. The laser Raman spectra were recorded on a Jobin-Yvon HR800 Raman spectrometer with a 12 mW He−Ne laser (632.8 nm). The exposition time is 10 s and accumulates twice. Weight changes of the products were measured out on a Thermal Analysis SDT Q600 analyzer from 25 to 1000 °C under an air atmosphere at a heating rate of 10 °C/min.

The hydrogenation of benzene was carried out in a quartz glass reactor under atmospheric pressure at 90 °C. The flow of benzene, controlled by a microsyringe pump at a flow rate of 5.6 mmol/h, was carried by H_2 with a gas flow rate of 10 mL/min and N_2 with a gas flow rate of 40 mL/min. For each experiment, 0.10 g of unreduced catalyst was loaded into the flow reactor. Before the reaction, the catalyst was reduced under a hydrogen (30 mL/min) and nitrogen (20 mL/min) mixture at 350 °C for 80 min. The product streams were analyzed by online gas chromatography equipped with a flame ionization detector.

Results and Discussion

Highly ordered Zr-based mesoporous materials are synthesized via the EISA method with amphiphilic triblock copolymers

SCHEME 1: Illustration of the Synthesis Procedure of Highly Ordered Mesoporous Zr-Based Materials

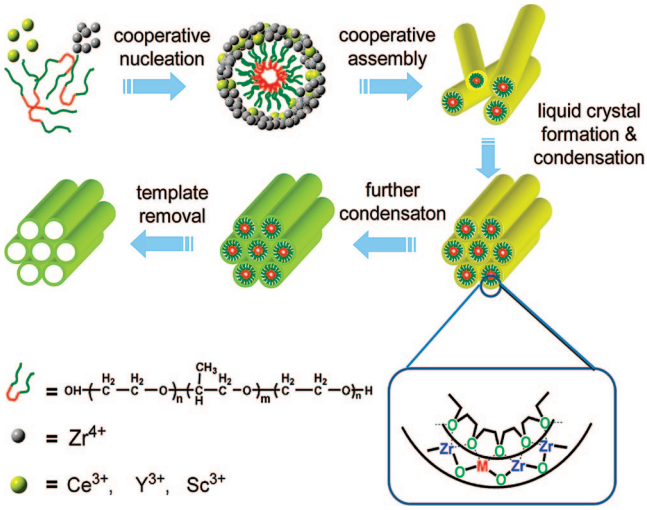

(PEO-PPO-PEO) as templates. Zirconium oxide chloride, metal nitrates, and metal alkoxides are chosen as cheap precursors, followed by a thermal process to remove the organic templates (Scheme 1). Our results demonstrate that the choice of zirconium oxide chloride is a key to the successful organization of the ordered mesostructures. No mesostructure is obtained when zirconium oxide nitrate ($ZrO(NO_3)_2 \cdot 5H_2O$) is used, with an obvious phase separation in the self-assembly process. In our synthesis, the chloride ions provided by the precursor can interact strongly with the inorganic species at the organic−inorganic interface and play an important role in the self-assembly process. In most cases with the traditional EISA strategy to fabricate mesoporous metal oxides, acids such as HCl, HNO_3, and H_3PO_4 are often necessary to slow down the hydrolysis−condensation rate of the metal precursors, avoiding the production of undesirable macroscale phase separation instead of robust mesostructures.[29] Interestingly, in the present work no extra acid is added, but this does not mean that the hydrolysis and condensation process is uncontrolled. The hydrolysis of zirconium oxide chloride and metal nitrate or metal alkoxide engenders an acidic ambience (pH 2) for the self-assembly process and acts as the inhibitor of the hydrolysis−condensation process of metal species. The condensation and polymerization rates are different for different metal species. The acidic condition slows down the cross-linking rate of the doped metal species, resulting in a simultaneous condensation−polymerization process of different metal species. The final nanocomposites have a uniform and homogeneous framework with well-dispersed multiple components in which oligomers of both zirconate and doped metal species cross-link together and construct the mesostructured frameworks without phase separation. Compared with zirconium alkoxide or zirconium chloride, which is commonly used as precursors in the synthesis of mesoporous zirconia, zirconium oxide chloride is much cheaper and is easily obtained, promising a low-cost fabrication of mesoporous Zr-based functional materials.

Amphiphilic triblock copolymers with different hydrophilic/hydrophobic groups such as P123 ($EO_{70}PO_{20}EO_{70}$) and F127 ($EO_{106}PO_{20}EO_{106}$) are used as the templates. To synchronize the assembly of the oligomers of zirconate and doped metal species, the amounts of copolymers are finely tuned, corresponding to the different doped metal species and different M/Zr (M = Ce, Y, Sc) ratios. In addition, the relative humidity and the evaporation temperature of the ambient atmosphere are important factors in the formation of mesostructures. A relative humidity of 50% and an evaporation temperature of 40 °C are adopted as typical conditions for the synthesis of all of the well-organized mesotructures with crystalline frameworks, indicating that the conditions above are feasible.

Mesoporous ZrO_2 (denoted as meso-ZrO_2) is also synthesized in ethanol solution with triblock copolymer F127 as the SDA.

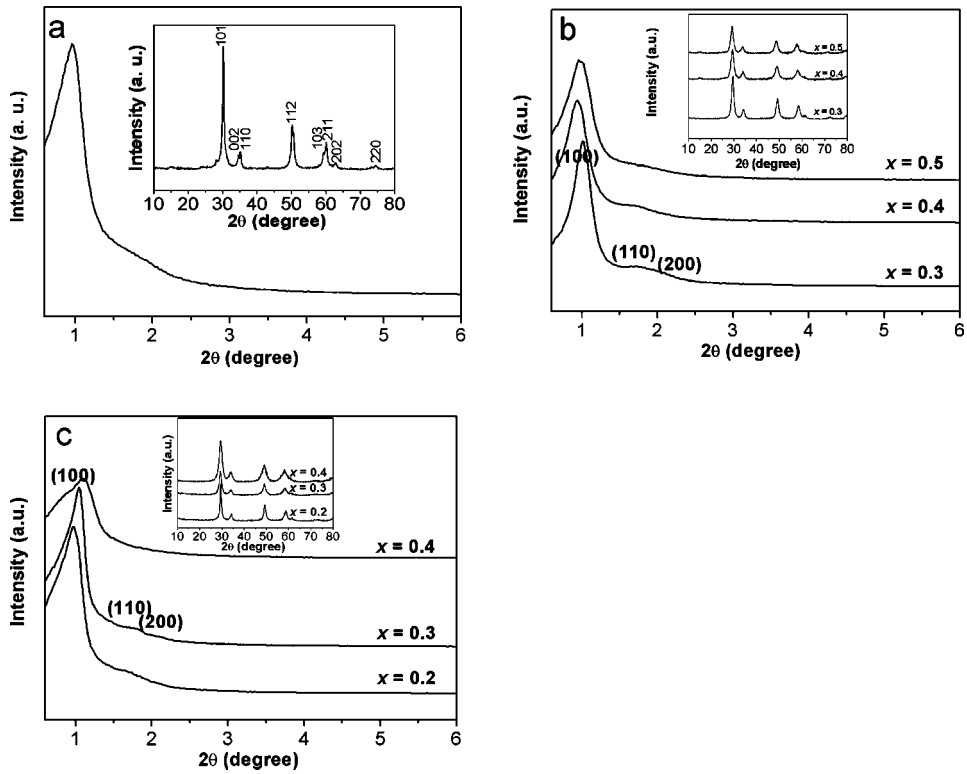

Figure 1. Small- and wide-angle XRD patterns of (a) meso-ZrO_2, (b) meso-CZ-P123, and (c) meso-CZ-F127 calcined at 400 °C.

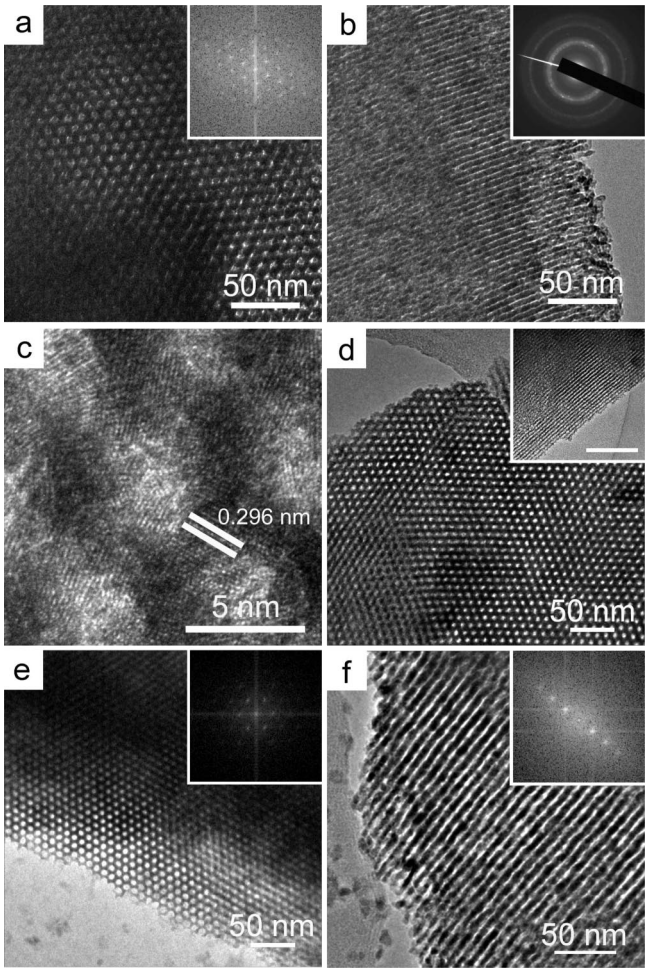

Figure 2. TEM images (a, b) of meso-ZrO_2 calcined at 400 °C as viewed along the [001] and [110] orientations (inset in image a is an FFT diffractogram and that in image b is the corresponding SAED pattern), HRTEM image (c) of meso-ZrO_2 calcined at 400 °C, TEM image (d) of meso-$Ce_{0.3}Zr_{0.7}O_2$−P123 calcined at 400 °C as viewed along the [001] orientation (inset in image d is a TEM image viewed along the [110] orientation), and TEM images (e, f) of meso-$Ce_{0.3}Zr_{0.7}O_2$−F127 calcined at 400 °C as viewed along the [001] and [110] orientations (FFT diffractogram inset). The bars are 100 nm for the insets.

The small-angle XRD pattern (Figure 1a) shows one diffraction peak at $2\theta = 0.96°$. In addition, one poorly resolved diffraction peak around 1.8° is observed. It is known that zirconia exists in three different crystalline structures: cubic, tetragonal, and monoclinic phases. Normally, the monoclinic phase is thermodynamically stable at room temperature whereas the tetragonal and cubic phases exist only at high temperature above 1170 and 2380 °C, respectively.[30] Unfortunately, these two high-temperature phases, which are more valuable for the technological applications mentioned above than the monoclinic phase, are unstable in bulk forms at ambient temperature. Garvie[31] predicted that pure ZrO_2 is stabilized in the tetragonal form at room temperature when the particle size is less than 30 nm. The wide-angle XRD pattern (inset in Figure 1a) of as-synthesized mesoporous ZrO_2 is indexed to the tetragonal phase (JCPDS card no. 80-0784), as further confirmed by Raman spectra detection (Figure S1 in Supporting Information) with the typical Raman activation mode of the tetragonal phase at 152, 260, 346, 440, 540, and 655 cm^{-1}.

The TEM images and corresponding fast Fourier transform (FFT) patterns (Figure 2a,b) reveal a high degree of periodicity over large domains, as viewed along the [001] and [110] orientations. The high-resolution TEM (HRTEM) image (Figure 2c) shows that the walls are highly crystalline with a lattice spacing of 0.296 nm, agreeing well with the value of 0.296 nm for the (101) planes of *t*-ZrO_2, which is confirmed by selected-area electron diffraction (SAED, inset of Figure 2b). The ordered mesoporous structure of ZrO_2 is not resistant to high temperature up to 600 °C (Figure S2a in Supporting Information). With the increase in calcination temperature, the nanocrystallites grow rapidly; meanwhile, a phase transformation occurs from tetragonal to monoclinic. Both monoclinic and tetragonal phases are observed when the sample is calcined at 600 °C (Figures S1 and S2b in Supporting Information), leading to the collapse of pore walls.

TABLE 1: Physicochemical Properties of Mesostructured Zr-Based Materials

sample	calcination temperature (°C)	BET surface area (m^2/g)	pore size (nm)	pore volume (cm^3/g)
meso-ZrO_2	400	97	4.1	0.14
meso-$Ce_{0.5}Zr_{0.5}O_2$-P123	400	132	3.7	0.19
meso-$Ce_{0.3}Zr_{0.7}O_2$-F127	400	128	4.1	0.18
	400	151	3.4	0.16
meso-10YZ	600	102	3.6	0.13
	700	55	3.2	0.06
meso-4SZ	400	137	4.0	0.19
meso-8SZ		186	3.5	0.28
meso-12SZ		188	3.6	0.24
meso-16SZ		217	3.4	0.20
meso-20SZ		216	3.3	0.21

CeO_2−ZrO_2 solid solutions with highly ordered mesostructures are fabricated using either P123 or F127 as SDAs (denoted as meso-CZ-P123 and meso-CZ-F127, respectively). The small-angle XRD patterns (Figure 1b,c) elucidate that long-range-ordered mesostructure is achieved over a wide Ce/Zr ratio range. The hexagonally packed cylindrical pores are clearly observed from TEM photographs (Figure 2d−f).

The nitrogen adsorption−desorption analysis show that mesoporous CeO_2−ZrO_2 solid solutions, compared with meso-ZrO_2, exhibit a higher BET surface area (Table 1) and a narrower pore size distribution (Figure S3 in Supporting Information), indicating a more uniform pore structure with cerium introduced. Besides, the obtained meso-CZ using poly(alkylene oxide) block copolymers with different hydrophilic/hydrophobic group ratios (P123 and F127) possess an approximate pore size of about 3 to 4 nm (Table 1). In the self-assembly process, the poly(ethylene oxide) (PEO) segments are incorporated into the rigid ceria−zirconia matrix whereas the poly(propylene oxide) (PPO) segments form the rigid hydrophobic core.[32] High-molecular-weight copolymers with long hydrophobic segments are promising candidates to template the large-pore mesoporous materials because the pore dimensions are mainly related to the length of the hydrophobic segments (here, they are related to the length of the PPO segments).[33−35] P123 and F127 have an equal number of PPO segments, resulting in the approximate scales of hydrophobic cores. After the polymers are removed by calcination, the pore sizes are almost the same.

Using the same synthesis strategy, we obtain yttria-stabilized zirconia with ordered mesostructure (denoted as meso-YZ) via replacing cerium nitrate with yttrium nitrate only. Ordered meso-YZ is synthesized over a relatively wide range of F127 concentration with a reactant composition (molar ratio) of F127/$Y(NO_3)_3 \cdot 6H_2O$/$ZrOCl_2 \cdot 8H_2O$/ethanol = y/0.20−1.7/3.3−4.8/2.5, where $y = 0.040$−0.079. Figure 3a shows the small-angle XRD patterns of mesoporous $(Y_2O_3)_{0.1}(ZrO_2)_{0.9}$ (denoted as

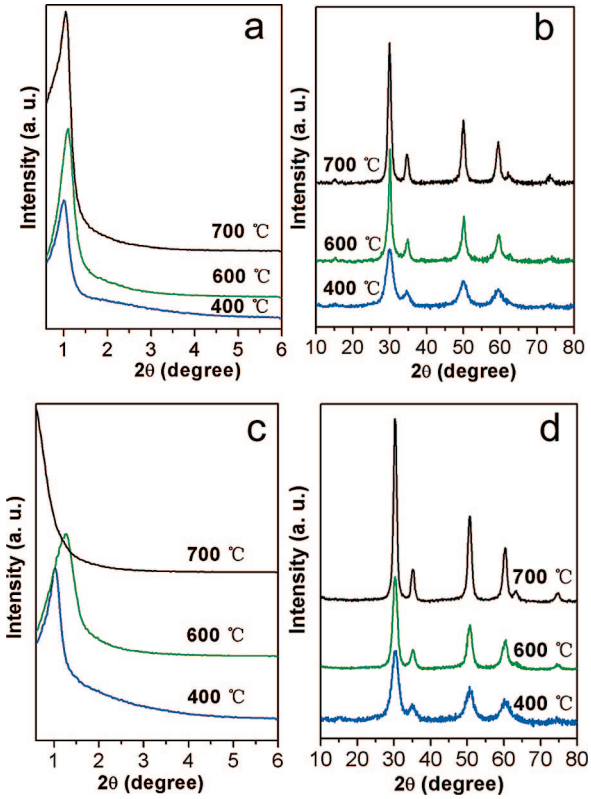

Figure 3. Small- (a) and wide-angle (b) XRD patterns of meso-10YZ calcined at different temperatures and small- (c) and wide-angle (d) XRD patterns of meso-10SZ calcined at different temperatures.

meso-10YZ) calcined at different temperatures. The combination of the small-angle and wide-angle XRD data convinces us of its high thermal stability by the fact that the ordered mesoporous structures with crystalline walls are retained even when calcined at 700 °C. The lattice parameters calculated from the small-angle XRD patterns of meso-10YZ calcined at 400, 600, and 700 °C are 8.8, 8.2, and 8.4 nm, respectively, suggesting slight framework shrinkage. We postulate that the introduction of yttrium enhances the thermal stability of mesostructure by cutting down the growth rate of nanocrystallites and inhibiting from the phase transformation. Similarly, mesoporous $(Sc_2O_3)_{0.1}(ZrO_2)_{0.9}$ (denoted as meso-10SZ) is also successfully synthesized (Figure 3b).

TEM images and corresponding FFT patterns are depicted in Figure 4. The TEM and FFT analyses confirm the presence of the well-defined long-range hexagonal arrangement of the pore channels in meso-10YZ (Figure 4a−c) and meso-10SZ (Figure 4e−f) and the fact that the ordered structures are retained even under heat treatment at high temperatures. The uniform, spherical large mesopores are clearly visible in these images. The cell parameters estimated from TEM images of meso-10YZ calcined at 400 and 600 °C are about 9 and 8 nm, respectively, in good agreement with those deduced from the small-angle XRD patterns. Additional proof for the crystallinity of the framework walls of meso-10YZ calcined at 600 °C is given by an HRTEM investigation (Figure 4d) that reveals the existence of several nanocrystallites with well-defined lattice planes, which is confirmed by selected-area electron diffraction (SAED, inset of Figure 4c). The nanocrystallite size is estimated to be about 3 to 4 nm whereas the wall is rather thick, roughly measured to be about 4 to 5 nm (obtained from XRD and nitrogen physisorption results).

The nitrogen sorption isotherms of meso-10YZ calcined at different temperatures show typical type IV curves with an H1-

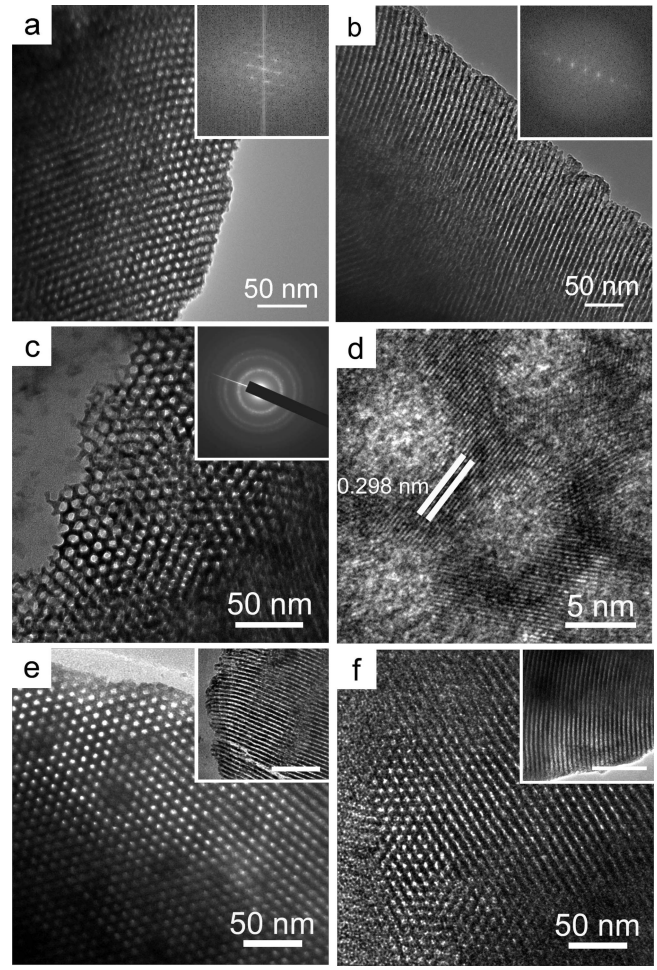

Figure 4. TEM images (a, b) of meso-10YZ calcined at 400 °C viewed along the [001] and [110] orientations (inset in image c corresponding to FFT diffractogram), TEM (c) and HRTEM (d) images of meso-10YZ calcined at 600 °C as viewed along the [001] orientation (SAED pattern in image c inset), TEM image of meso-10SZ calcined at 400 (e) and 600 °C (f) as viewed along the [001] orientation (TEM images viewed along the [010] orientation in the inset). The bars are 100 nm for the insets.

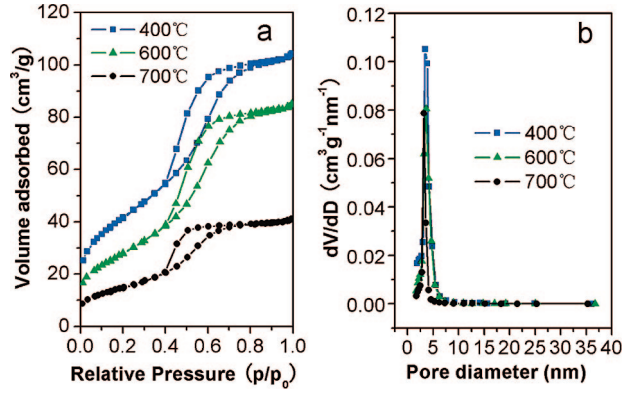

Figure 5. (a) Nitrogen adsorption−desorption isotherms and (b) pore size distribution curves (deduced from the desorption branches) of meso-10YZ calcined at different temperatures.

type hysteresis loop as defined by IUPAC and a distinct condensation step over a P/P_0 range of 0.4−0.8, suggesting a uniform cylindrical mesopore channel (Figure 5a). It can be calculated from the nitrogen desorption branch that meso-10YZ calcined at 400 °C has a BET surface area of 151 m^2/g and a pore volume of 0.16 cm^3/g (Table 1). The pore size distribution

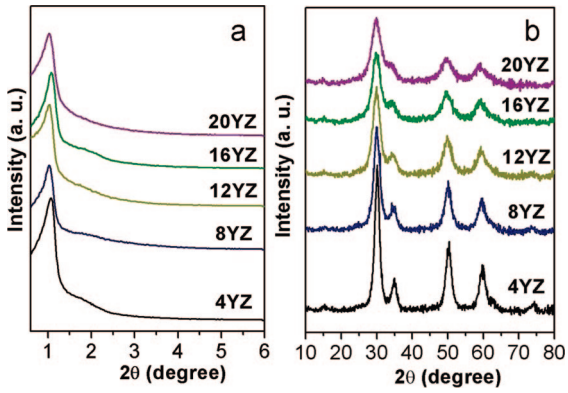

Figure 6. Small- (a) and wide-angle (b) XRD patterns of meso-YZs with different Y/Zr ratios.

calculated with the Barrett−Joynes−Halenda (BJH) method is quite narrow (Figure 5b), indicating a uniform pore structure with a pore diameter of 3.4 nm. During the calcination process from 400 to 700 °C, the pore size of meso-10YZ does not vary greatly (around 3.5 nm) whereas the BET surface area and pore volume decrease to 55 m^2/g and 0.06 cm^3/g, respectively.

Thermogravimetric differential thermal analysis (TG-DTA) profiles of the as-synthesized meso-ZrO_2 sample under an air atmosphere are given in Figure S4a. Two weight-loss stages are observed. The removal of physically adsorbed water is observed below 100 °C whereas the dehydration of zirconium hydroxide and transformation to crystalline zirconia occur within 150−400 °C. A remarkable exothermic effect centered at 300 °C is shown in the DTA curve, accompanied by a significant weight loss of about 35 wt % from 200 to 300 °C. This weight loss is mainly attributed to the decomposition of amphiphilic triblock copolymer F127. The as-synthesized meso-10YZ sample heated under an air atmosphere exhibits three significant exothermic peaks (Figure S4b) in DTA curve. The first one centered at 170 °C is attributed to the dehydration of the as-synthesized sample, and the second one centered at 350 °C correlates to the combination of the decomposition of F127 and the crystallization of the pore walls. Different from meso-ZrO_2, as-synthesized meso-10YZ shows a remarkable exothermic effect centered at 500 °C due to the further crystallization of the pore walls. It is noted that the thermal effect during the crystallization is continuous and smooth and then results in the higher thermal stability of the ordered mesoporous structure. We postulate that it is ascribed to the introduced yttrium that inhibits the nanocrystallite growth. From the TG curve, we can evaluate that the weight loss before 200 °C is 30 wt % and that in the range of 200−500 °C is 40 wt %.

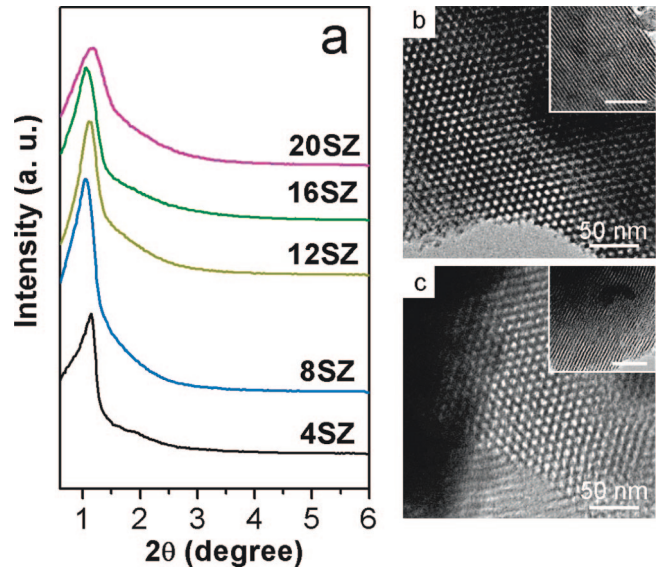

Figure 8. Small-angle XRD patterns of meso-SZs with different Sc/Zr ratios (a) and TEM images of meso-4SZ (b) and meso-12SZ (c) viewed along the [001] orientation. (The insets are TEM images viewed along the [010] orientation.) The bars are 100 nm for the insets.

By carefully adjusting the quantity of SDAs, a series of highly ordered mesoporous yttria-stabilized zirconia with x in $(Y_2O_3)_x(ZrO_2)_{1-x}$ ranging from 0.04 to 0.20 are successfully synthesized, which is proven by the small-angle XRD patterns shown in Figure 6. They all exhibit a very strong diffraction peak at around 1.0°, and one weak peak around 1.7° is also observed in the patterns of 4YZ, 8YZ, 12YZ, and 20YZ, indicating a highly ordered periodicity. The representative TEM images of meso-4YZ, 8YZ, and 20YZ displayed in Figure 7 reveal that they all possess 2D hexagonal symmetry.

A series of scandia-stabilized zirconia with ordered mesostructure (denoted as meso-SZ) are obtained in the same way. The combination of small-angle XRD patterns (Figure 8a) and representative TEM images of meso-4SZ and 12SZ (Figure 8b,c) confirms the existence of uniform pore channels. For zirconia, the tetragonal ($P4_2/nmc$) phase is slightly distorted from the cubic phase ($Fm-3m$). The broadening of the reflections in wide-angle XRD patterns (Figure 9a) obviously indicates the nanocrystalline nature of as-prepared samples and thus makes it difficult to differentiate between these two crystal phases. Therefore, Raman spectroscopy, as an effective tool for detecting the crystal structure of fine particles, is utilized to determine the exact phases of our meso-SZ samples. Figure 9b is the vis−Raman spectra of the meso-SZ samples. For the meso-4SZ sample, five Raman peaks are located at 150, 263, 332,

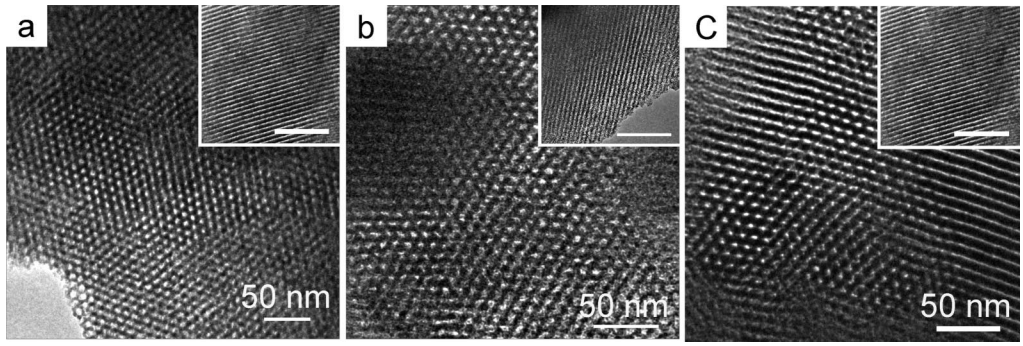

Figure 7. TEM images of meso-4YZ (a), meso-8YZ (b), and meso-20YZ (c) as viewed along the [001] orientation. (The insets are TEM images viewed along the [010] orientation.) The bars are 100 nm for the insets.

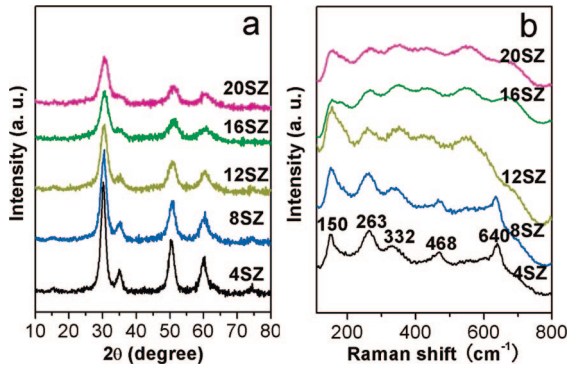

Figure 9. Wide-angle XRD patterns (a) and Raman spectra (b) of meso-SZs with different Sc/Zr ratios.

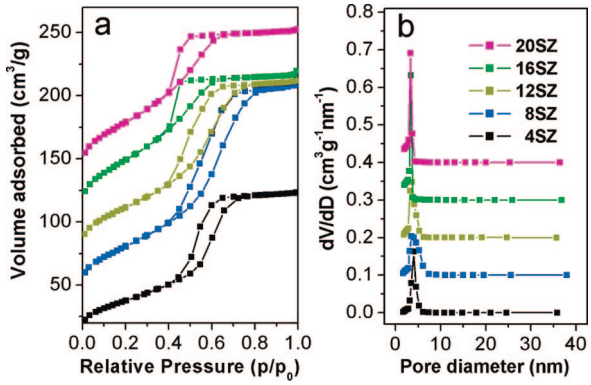

Figure 10. Nitrogen adsorption−desorption isotherms (a) and pore size distribution curves (deduced from the desorption branches) (b) of meso-SZs with different Sc/Zr ratios. For clarity, the isotherms for 8SZ, 12SZ, 16SZ, and 20SZ in plot a are offset along the *y* axis by 30, 60, 90, and 120 cm^3/g, respectively.

468, and 640 cm^{-1} plus one shoulder at ca. 602 cm^{-1}, consisting of the six Raman-active modes ($A_{1g} + 2B_{1g} + 3E_g$) of *t*-ZrO_2 and revealing the characteristic of its stable tetragonal phase.[37] Sample meso-8SZ also exhibits the Raman peaks corresponding to the typical tetragonal phase. As the quantity of scandium increases, the intensities of all peaks decrease, and the peaks become broader, presenting the characteristic of the cubic phase.[38,39] As for the samples of meso-12SZ, 16SZ, and 20SZ, a mixture of tetragonal and cubic phases or a transitional metastable phase is determined on the basis of the Raman bands at ca. 150, 263, 332, and 468 cm^{-1} and broad bands from 530 to 640 cm^{-1}.[38,39]

All of the nitrogen sorption isotherms of meso-SZ calcined at 400 °C with different Sc/Zr ratios show representative type IV curves with sharp capillary condensation steps (Figure 10a). The pore-size distributions determined by using a BJH analysis show narrow peaks around 3 to 4 nm (Figure 10b). The BET surface areas and pore volumes of meso-SZ are measured to be 130−220 m^2/g and 0.19 − 0.28 cm^3/g, respectively (Table 1). The results indicate that all meso-SZs with different Sc/Zr ratios possess uniform monodisperse mesopore sizes.

Representative well-ordered mesoporous ZrO_2 and $Ce_{0.5}Zr_{0.5}O_2$ are examined as catalyst supports in the hydrogenation of benzene to cyclohexane. Loading with 4.5 wt % Ru, the Ru/meso-ZrO_2 and Ru/meso-$Ce_{0.5}Zr_{0.5}O_2$ catalysts are employed for the hydrogenation of benzene at a temperature of 90 °C. The evolution of the benzene conversion as a function of time is presented in Figure 11. It can be seen that almost 13% for both catalysts is obtained and the conversion rate decreases slowly along with the reaction time, indicating the good stability of

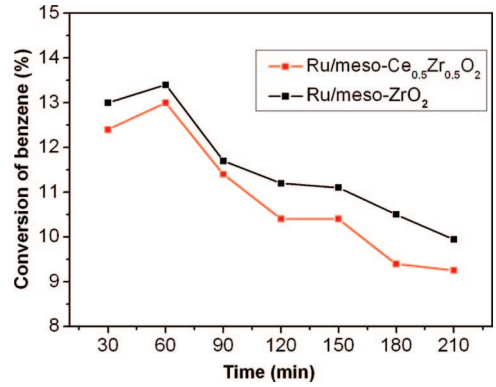

Figure 11. Benzene conversion achieved over Ru/meso-ZrO_2 and Ru/meso-$Ce_{0.5}Zr_{0.5}O_2$ at a temperature of 90 °C.

the catalysts. Therefore, these results strongly suggest that these ordered mesoporous Zr-based supports should have potential applications in catalytic fields.

Conclusions

In summary, we have developed a facile and widely applicable method for the synthesis of Zr-based multicomponent functional materials with highly ordered mesoporous structures from the combination of inexpensive and commercially available polymers with metal inorganic salts solubilized in ethanol solution. Herein, all of the hydrolysis, condensation, and assembly processes are self-adjusting without additional acid or base. Pure zirconia, ceria−zirconia solid solutions, yttria-stabilized zirconia, and scandia-stabilized zirconia with well-organized pore structures are all obtained via this facile synthesis method. The mesoporous materials above have large surface areas, tunable pore sizes, crystalline framworks, multiple components, a high degree of homogeneity, and, in certain cases, thermal stability up to 700 °C, which presents advantages for commercial applications in heterogeneous catalysts, SOFC, and oxygen sensors. Most importantly, using this "self-adjusting" method, the diverse hydrolysis−condensation kinetics of various metal oxides is homogenized to yield stable multicomponent precursors. The development of such a simple and widely applicable method for the fabrication of novel mesoporous functional materials with diverse compositions is important for practical applications. Loaded with ruthenium, the representative mesoporous ZrO_2 and $Ce_{0.5}Zr_{0.5}O_2$ exhibit catalytic activity in the hydrogenation of benzene, indicating the potential applications in catalysis.

Acknowledgment. This work was supported by the MOST of China (2006CB601104) and the NSFC (20821091, 20671005, 20771009, and 20731160001).

Supporting Information Available: Raman spectra of meso-ZrO_2; small- and wide-angle XRD patterns of meso-ZrO_2 calcined at 600 °C; nitrogen adsorption−desorption isotherms and corresponding pore size distribution curves (deduced from the desorption branches) of meso-$Ce_{0.3}Zr_{0.7}O_2$−F127; TG-DTA profiles for the as-synthesized meso-ZrO_2 and meso-10YZ; and EDX data of meso-ZrO_2, meso-10YZ, and meso-10SZ. This material is available free of charge via the Internet at http://pubs.acs.org.

References and Notes

(1) Badwal, S. P. S. *Appl. Phys. A: Mater. Sci. Process.* **1990**, *50*, 449.

(2) Garvie, R. C.; Hannink, R. H.; Pascoe, R. T. *Nature* **1975**, *258*, 703.
(3) Murase, Y.; Kato, E. *J. Am. Ceram. Soc.* **1982**, *66*, 196.
(4) Phillips, J. M. *J. Appl. Phys.* **1996**, *79*, 1829.
(5) León, C.; Lucía, M. L.; Santamaría, J. *Phys. Rev. B* **1997**, *55*, 882.
(6) Mansour, N.; Mansour, K.; Stryland, E. W. V.; Soileau, M. J. *J. Appl. Phys.* **1990**, *67*, 1475.
(7) (a) Wilk, G. D.; Wallace, R. M.; Anthony, J. M. *J. Appl. Phys.* **2001**, *89*, 5243. (b) Afanas'ev, V. V.; Houssa, M.; Stesmans, A.; Heyns, M. M. *Appl. Phys. Lett.* **2001**, *78*, 3073.
(8) Tanabe, K. *Mater. Chem. Phys.* **1985**, *13*, 347.
(9) Yamaguchi, T. *Catal. Today* **1994**, *20*, 199.
(10) (a) Kašpar, J.; Fornasiero, P.; Graziani, M. *Catal. Today* **1999**, *50*, 285. (b) Kašpar, J.; Fornasiero, P.; Hickey, N. *Catal. Today* **2003**, *77*, 419.
(11) Fornasiero, P.; Balducci, G.; Di Monte, R.; Kašpar, J.; Sergo, V.; Gubitosa, G.; Ferrero, A.; Graziani, M. *J. Catal.* **1996**, *164*, 173.
(12) (a) Weing, W.; Yang, J.; Ding, Z. *J. Non-Cryst. Solids* **1994**, *169*, 177. (b) Zhang, Y. W.; Jin, S.; Yang, Y.; Li, G. B.; Tian, S. J.; Jia, J. T.; Liao, C. S.; Yan, C. H. *Appl. Phys. Lett.* **2000**, *77*, 3409. (c) Zhang, Y. W.; Yang, Y.; Jin, S.; Tian, S. J.; Li, G. B.; Jia, J. T.; Liao, C. S.; Yan, C. H. *Chem. Mater.* **2001**, *13*, 372.
(13) (a) Kresge, C. T.; Leonowicz, M. E.; Roth, W. J.; Vartuli, J. C.; Beck, J. S. *Nature* **1992**, *359*, 710. (b) Beck, J. S.; Vartul, J. C.; Roth, W. J.; Leonowicz, M. E.; Kresge, C. T.; Schmitt, K. D.; Chu, C. T.-W.; Olson, D. H.; Sheppard, E. W.; McCullen, S. B.; Higgins, J. B.; Schlenkert, J. L. *J. Am. Chem. Soc.* **1992**, *114*, 10834.
(14) He, X.; Antonelli, D. *Angew. Chem., Int. Ed.* **2002**, *41*, 214.
(15) Xiao, F. S. *Top. Catal.* **2005**, *35*, 9.
(16) (a) Morris, C. A.; Anderson, M. L.; Stroud, R. M.; Merzbacher, C. I.; Rolison, D. R. *Science* **1999**, *284*, 622. (b) Carreon, M. A.; Guliants, V. V. *Eur. J. Inorg. Chem.* **2005**, 27.
(17) Corma, A. *Chem. Rev.* **1997**, *97*, 2373.
(18) Bartl, M. H.; Boettcher, S. W.; Frindell, K. L.; Stucky, G. D. *Acc. Chem. Res.* **2005**, *38*, 263.
(19) Grosso, D.; Boissière, C.; Smarsly, B.; Brezesinski, T.; Pinna, N.; Albouy, P. A.; Amenitsch, H.; Antonietti, M.; Sanchez, C. *Nat. Mater.* **2004**, *3*, 787.
(20) (a) Lu, A. H.; Schüth, F. *Adv. Mater.* **2006**, *18*, 1793. (b) Lee, J.; Kim, J.; Hyeon, T. *Adv. Mater.* **2006**, *18*, 2073.
(21) (a) Jiao, F.; Shaju, K. M.; Bruce, P. G. *Angew. Chem., Int. Ed.* **2005**, *44*, 6550. (b) Luo, J. Y.; Wang, Y. G.; Xiong, H. M.; Xia, Y. Y. *Chem. Mater.* **2007**, *19*, 4791.
(22) Fan, J.; Boettcher, S. W.; Stucky, G. D. *Chem. Mater.* **2006**, *18*, 6391.
(23) (a) Yang, P. D.; Zhao, D. Y.; Margolese, D. I.; Chmelka, B. F.; Stucky, G. D. *Nature* **1998**, *396*, 152. (b) Yang, P. D.; Zhao, D. Y.; Margolese, D. I.; Chmelka, B. F.; Stucky, G. D. *Chem. Mater.* **1999**, *11*, 2813.
(24) Ciesla, U.; Fröba, M.; Stucky, G. D.; Schüth, F. *Chem. Mater.* **1999**, *11*, 227.
(25) (a) Mamak, M.; Coombs, N.; Ozin, G. *Adv. Mater.* **2000**, *12*, 198. (b) Mamak, M.; Coombs, N.; Ozin, G. *J. Am. Chem. Soc.* **2000**, *122*, 8932. (c) Mamak, M.; Coombs, N.; Ozin, G. *Chem. Mater.* **2001**, *13*, 3564.
(26) Wang, Y. Q.; Yin, L. X.; Palchik, O.; Hacohen, Y. R.; Koltypin, Y.; Gedanken, A. *Chem. Mater.* **2001**, *13*, 1248.
(27) Crepaldi, E. L.; Soler-Illia, G. J. A. A.; Bouchara, A.; Grosso, D.; Durand, D.; Sanchez, C. *Angew. Chem., Int. Ed.* **2003**, *42*, 347.
(28) Yuan, Q.; Liu, Q.; Song, W. G.; Feng, W.; Sun, L. D.; Zhang, Y. W.; Yan, C. H. *J. Am. Chem. Soc.* **2007**, *129*, 6698.
(29) Soler-Illia, G. J. A. A.; Sanchez, C.; Lebeau, B.; Patarin, J. *Chem. Rev.* **2002**, *102*, 4093.
(30) Li, L. R.; Wang, W. Z. *Solid State Commun.* **2003**, *127*, 639.
(31) Garvie, R. C. *J. Phys. Chem.* **1978**, *82*, 218.
(32) Boettcher, S. W.; Bartl, M. H.; Hu, J. G.; Stucky, G. D. *J. Am. Chem. Soc.* **2005**, *127*, 9721.
(33) Kramer, E.; Forster, S.; Goltner, C.; Antonietti, M. *Langmuir* **1998**, *14*, 2027.
(34) Yu, K.; Hurd, A. J.; Eisenberg, A.; Brinker, C. J. *Langmuir* **2001**, *17*, 7961.
(35) Smarsly, B.; Xomeritakis, G.; Yu, K.; Liu, N.; Fan, H.; Roger, A.; Assink, R. A.; Drewien, C. A.; Ruland, W.; Brinker, C. J. *Langmuir* **2003**, *19*, 7295.
(36) López, E. F.; Escribano, V. S.; Panizza, M.; Carnasciali, M. M.; Busca, G. *J. Mater. Chem.* **2001**, *11*, 1891.
(37) Martínez-Arias, A.; Fernández-García, M.; Ballesteros, V.; Salamanca, L. N.; Conesa, J. C.; Otero, C.; Soria, J. *Langmuir* **1999**, *15*, 4796.
(38) Cai, J.; Raptis, C.; Raptis, Y. S.; Anastassakis, E. *Phys. Rev. B.* **1995**, *51*, 201.
(39) Morell, G.; Kutiyar, R. S.; Torres, D.; Paje, S. E.; Llopis, J. *J. Appl. Phys.* **1997**, *81*, 2830.

JP806467C